

# A Novel Inertial-Visual Heading Determination System for Wheeled Mobile Robots

Wenjun Lv<sup>1</sup>, Member, IEEE, Yu Kang<sup>1</sup>, Senior Member, IEEE, Yun-Bo Zhao<sup>1</sup>, Senior Member, IEEE, Yuping Wu<sup>1</sup>, Graduate Student Member, IEEE, and Wei Xing Zheng<sup>2</sup>, Fellow, IEEE

**Abstract**—Finding an alternative way to replace the magnetic compass to determine the robot heading angle indoor is always a challenge in the robotics society. This brief proposes a structurally simple yet efficient nonmagnetic heading determination system, which can be used in the planar indoor environment with abundant ferromagnetic and electromagnetic interferences, by the combination of gyroscope and vision. The gyroscope is utilized to perceive the yaw rate, whereas a downward-looking camera is used to capture the pre-laid auxiliary strips to acquire the absolute angle of the robot heading. Due to the existence of pseudomeasurement, varying noise statistical characteristics, and asynchronization between state propagation and measurement, the existing Kalman filters cannot be applied to fuse the gyroscopic and visual data. Therefore, a novel fusion algorithm named pseudomeasurement-resistant adaptive asynchronous Kalman filter is proposed, which is experimentally verified to be efficient in the environment with various interferences.

**Index Terms**—Gyroscope, heading determination system (HDS), Kalman filter, magnetic compass, vision.

## I. INTRODUCTION

THE recent decades have witnessed the development of wheeled mobile robots and their applications in military, rescue, service, transport, warehousing, and so on. One of the fundamental problems in mobile robotics is mobility, which enables robots to move from location to location [1]. To realize

Manuscript received June 21, 2019; revised November 15, 2019 and March 10, 2020; accepted July 22, 2020. Date of publication August 7, 2020; date of current version June 10, 2021. Manuscript received in final form July 24, 2020. This work was supported in part by the National Natural Science Foundation of China under Grant 61903353, Grant 61725304, and Grant 61673361; in part by the National Key Research and Development Project of China under Grant 2018AAA0100800 and Grant 2018YFE0106800, in part by the Major Science and Technology Project of Anhui Province under Grant 912198698036, in part by the SINOPEC Programmes for Science and Technology Development under Grant PE19008-8, and in part by the Fundamental Research Funds for the Central Universities under Grant WK2100000013. Recommended by Associate Editor X. Chen. (Corresponding author: Yu Kang.)

Wenjun Lv and Yun-Bo Zhao are with the Department of Automation, University of Science and Technology of China, Hefei 230027, China (e-mail: wlv@ustc.edu.cn; ybzhao@ieee.org).

Yu Kang is with the Department of Automation, University of Science and Technology of China, Hefei 230027, China, also with the State Key Laboratory of Fire Science, University of Science and Technology of China, Hefei 230027, China, and also with the Institute of Advanced Technology, University of Science and Technology of China, Hefei 230027, China (e-mail: kangduyu@ustc.edu.cn).

Yuping Wu is with the College of Information Engineering, Zhejiang University of Technology, Hangzhou 310023, China (e-mail: ypwu@zjut.edu.cn).

Wei Xing Zheng is with the School of Computer, Data and Mathematical Sciences, Western Sydney University, Sydney, NSW 2751, Australia (e-mail: w.zheng@westernsydney.edu.au).

Color versions of one or more of the figures in this article are available online at <https://ieeexplore.ieee.org>.

Digital Object Identifier 10.1109/TCST.2020.3012380

the location-to-location transferability, the robot should be able to efficiently control its wheel rotational rates to track the planned route [2]. During the tracking control, the robot should accurately obtain its pose (i.e., the 2-D coordinate and heading angle) in real time, thus forming a closed-loop system [3]. The localization problem has already been intensively investigated, while there is still room in the study of heading determination system (HDS), which will be discussed in this brief.

The robot localization can be achieved by resorting to various measures, such as satellite, Wi-Fi, vision, lidar, but the sensor to perceive the robot heading is almost unique, that is, magnetic compass [4]. The magnetic compass is usually realized by a magnetometer, which perceives the magnetic intensity along different axes, and thus, it is able to provide the heading angle relative to the north. Apart from the magnetic compass, the heading angle can be determined by a localization system. In outdoor scenarios, the dual-antenna GPS is able to calculate the robot heading by processing the baseline between the main antenna and the second one [5]. The similar HDS can be implemented by Wi-Fi localization in the indoor environments. As another nonmagnetic compass, one can use the vision, whether on-board or off-board, to capture the environmental or robotic markers and then determine the robot heading angle from the capture images. The state-of-the-art work related to the mentioned three HDSs is as follows.

The magnetic compass is generally considered to originate in the ancient China as early as the 206 B.C., so it has been used as a device to find the direction since the ancient times [6]. By perceiving the geomagnetic intensity, the magnetic compass could calculate the direction with respect to the north. However, in the environment with a large body of ferromaterial and electromaterial, the distorted magnetic field gives rise to the inaccuracy and unreliability in magnetic compass. In order to eliminate the errors rendered by hard- and soft-iron distortion magnetic field, we can calibrate the magnetometer in advance, by means of the vector compensation or ellipsoidal calibration [7]. The time-varying and unpredictable magnetic interference, however, limits the real-time application in the heading measurement of a mobile robot. A preferred solution is integrating a gyroscope, which is complementary to the magnetic compass. In [8], the regular and irregular noises of a magnetometer are filtered by a fuzzy-based compensator and the Kalman filter, respectively. Due to the insensitivity to magnetic interference, the gyroscope can be used to isolate the anomalies in the magnetometer readings, thus avoiding the pollution to heading estimation [9]. The aforementioned magnetometer-involved magnetic HDSs are usually

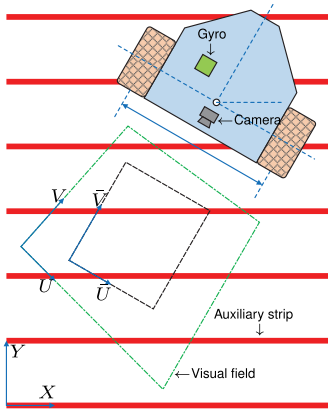


Fig. 1. Illustration of the proposed inertial-visual heading estimation system. The polygon in blue and the two meshed rectangles in yellow represent the robot body and its wheels. A gyroscope (green square) is mounted on the robot body with its axis vertical to the floor. The green dashed quadrilateral represents the visual field of the downward-looking camera. The red thicker lines, which are parallel to the  $X$ -axis, represent the auxiliary strips.

used in the scenarios without serious geomagnetic distortion. However, in some scenarios, especially the industrial environment, magnetic compass is extremely unwelcome and thus should be avoided [1].

Apart from the magnetic compass, the nonmagnetic HDS has attracted more and more attention in the current decade. The location-to-heading method implemented by GPS is called GPS compass, which is frequently used in outdoor vehicles [10]. The vehicle is desired to be moving as straightly as possible when using GPS compass to determine its heading, and otherwise, a large body of errors occurs. Therefore, such a method is not reliable if the vehicle moves irregularly [11]. Meanwhile, the nonline-of-sight communication may degrade the localization system and further reduce the accuracy of GPS compass. Another promising way to obtain the heading information is vision. With a dedicated colored marker sticking on the robot roof, one can use the off-board vision to monitor the robot and extract the robot pose from the captured image sequence [12]–[14]. However, the method fails if the robot runs out of the visual field or a table blocks the line of sight. On the contrary, the on-board vision utilizes a camera directly mounted on the robot to capture the landmarks distributed in the environment; and then, the robot location and heading could be worked out. The quick response codes are the most frequently used landmarks [15], which has received a great achievement in the warehousing robots [16].

In this brief, we propose a novel nonmagnetic way to determine the robot heading angle, which does not suffer from ferromagnetic and electromagnetic interferences. The system is shown in Fig. 1. The floor of the area that the robot operates should be laid with some auxiliary strips in advance. The floor should be flat, but moderate inclination and slippery are acceptable. All strips are parallel to the  $X$ -axis and equally spaced. The strips' color is optional, but complementary to the floor color in hue. The gyroscope is mounted on the robot with its axis perpendicular to the floor, thus perceiving the pure yaw rate of the robot. An on-board downward-looking

camera captures the floor images.<sup>1</sup> Because all the auxiliary strips are parallel to the  $X$ -axis, the relative angle between the robot heading and  $X$ -axis could be extracted from the floor images. By adjusting the camera pose, the area of visual field could be enlarged, and therefore, it can be guaranteed that the vision could capture one auxiliary strips at least.

In order to estimate the robot heading, we first establish the relationship from the angle of the captured strips in the image framework to the heading angle in the world framework, which enables the nonmagnetic way to perceive the absolute angle of the robot heading. However, the fusion of gyroscopic yaw rate and visual heading measurement is not a straightforward work by applying the Kalman filter, which is due to the following issues.

- 1) Because of the unknown direction of the auxiliary strips, the visual heading measurement outputs two values, a real measurement and a pseudo one.
- 2) Because of the camera shake and illumination variation, the noise variances, particularly the measurement noise variance, change slowly.
- 3) Because the visual heading measurement is time-consuming and resource-intensive, the gyroscopic state propagation proceeds at a higher rate than the visual measurement, which causes the asynchronization issue.

Although many modified Kalman filters have been proposed (e.g., robust Kalman filter [17], switch Kalman filter [18], and adaptive Kalman filter [19]), there does not exist such a Kalman filter capable of solving the aforementioned three issues, to the best of our knowledge. Therefore, a novel fusion algorithm named pseudomeasurement-resistant adaptive asynchronous Kalman filter is proposed in this brief.

In the rest of this brief, the models of the gyroscopic measurement of yaw rate and the visual measurement of robot heading will be presented in Section II, and the proposed pseudomeasurement-resistant adaptive asynchronous Kalman filter applying to the inertial-visual fusion will be stated in Section III. In Section IV, the real-world experiment is exhibited to verify the effectiveness of the inertial-visual HDS. This brief is concluded in Section V.

## II. MODELING OF SENSORS

### A. Gyroscopic Measurement of Yaw Rate

Gyroscope is a device sensing the rotational rate of a rigid body. If considering all error items, the model could be very complicated, so the model precision and complexity should be compromised. Because the systematic uncertainties could be precalibrated by experiments, only the nonsystematic items will be considered to establish a feasible gyroscopic error model [20]. A large body of experiments have demonstrated that the angular random walk (ARW) and angular rate random walk (ARRW) affect the gyroscopic accuracy significantly [21]. The ARW reflects the characteristics of white noise in the angular rate, so it can be seen as a fast-changing noise. Similarly, the ARRW reflects the characteristics of white

<sup>1</sup>The strips interval, camera's height, and posture could be adjusted jointly to guarantee that the camera captures at least one auxiliary strip at any location.

noise in the angular acceleration, so it is a slow-changing noise. According to the abovementioned analysis, we have the model that relates the real yaw rate to the gyroscopic readings, that is,

$$\delta_{g,k} = \delta_k + b_{g,k} + n_{g,k} \quad (1)$$

where  $\delta_k$  denotes the robot yaw rate,  $\delta_{g,k}$  denotes the gyroscopic readings, and  $b_{g,k}$  and  $n_{g,k}$  denote the ARRW and ARW error, respectively, all at sampling point  $k$ . The fast-changing noise  $n_{g,k}$  is modeled as Gaussian noise, i.e.,  $n_{g,k} \sim \mathcal{N}(0, Q_n)$ . Meanwhile, the slow-changing noise  $b_{g,k}$  is modeled as a one-order Markov–Gaussian stochastic process, that is,

$$b_{g,k+1} = \gamma b_{g,k} + w_{g,k} \quad (2)$$

where  $w_{g,k} \sim \mathcal{N}(0, Q_w)$  is the Gaussian noise and  $\gamma \in [0, 1]$  denotes the correlation coefficient, which indicates the correlation between two successive states. The correlation gets stronger with  $\gamma$  getting larger. Because the ARRW error changes very slowly, we often set  $\gamma = 1$  empirically.

### B. Visual Measurement of Heading

The visual heading measurement is implemented by the monocular vision with the aid of floor auxiliary strips. The process contains the following steps.

1) *Image Preprocess*: This step aims to extract the central lines of the auxiliary strips. First, the colored floor image is converted into a binary image with reserving the auxiliary strips, by using thresholding segmentation. Second, the binary image is further processed by using mathematical morphology (e.g., hole filling, skeleton extraction, and burring algorithm), thus obtaining the central lines of the auxiliary strips.

2) *Line Detection*: This step aims to acquire the parameters of the auxiliary strips in the  $U$ – $V$  framework by using the Hough transform and perspective transform. The auxiliary strips are parameterized by

$$u \cos \rho + v \sin \rho = r \quad (3)$$

where  $r \in [r_{\min}, r_{\max}]$  denotes the vertical distance from the origin of the  $U$ – $V$  framework to the strip's central line and  $\rho \in [-\pi/2, \pi/2)$  denotes the angle from the  $U$ -axis to the vertical line. For a  $\mu \times \nu$  image, we have  $r_{\max} = -r_{\min} = (\mu^2 + \nu^2)^{1/2}$ . The parameters  $(r, \rho)$  can be obtained by using the Hough transform.

3) *Perspective Transform*: Because the camera's optical axis may not be vertical to the floor, we should project the captured floor image onto the floor plane. Define the perspective transformation function

$$(\bar{u}, \bar{v}) = \mathfrak{P}\{(u, v)\} \quad (4)$$

where  $(u, v)$  is a point in the  $U$ – $V$  framework and  $(\bar{u}, \bar{v})$  is a point in the  $\bar{U}$ – $\bar{V}$  framework. More details of the perspective transform can be found in [22]. Now, we are in the position to convert  $(r, \rho)$ -lines into  $(\bar{r}, \bar{\rho})$ -lines in the  $\bar{U}$ – $\bar{V}$  framework. Find two points on the  $(r, \rho)$ -line, and calculate

$$(\bar{u}_1, \bar{v}_1) = \mathfrak{P}\{(u_1, v_1)\} \quad (5a)$$

$$(\bar{u}_2, \bar{v}_2) = \mathfrak{P}\{(u_2, v_2)\} \quad (5b)$$

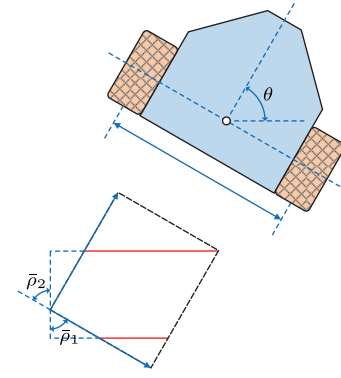


Fig. 2. Illustration of the relation of  $\bar{\rho}$  and  $\theta$  in Situation 1.

where  $(\bar{u}_1, \bar{v}_1)$  and  $(\bar{u}_2, \bar{v}_2)$  are two points on the  $(\bar{r}, \bar{\rho})$  line. Substituting them to (3) yields

$$\bar{u}_1 \cos \bar{\rho} + \bar{v}_1 \sin \bar{\rho} = \bar{r} \quad (6a)$$

$$\bar{u}_2 \cos \bar{\rho} + \bar{v}_2 \sin \bar{\rho} = \bar{r} \quad (6b)$$

and consequently, we have

$$\bar{\rho} = \begin{cases} \arctan \frac{\bar{u}_1 - \bar{u}_2}{\bar{v}_2 - \bar{v}_1}, & \text{when } \bar{v}_1 \neq \bar{v}_2 \\ -\frac{\pi}{2}, & \text{when } \bar{v}_1 = \bar{v}_2 \end{cases} \quad (7)$$

which realizes the conversion from the  $U$ – $V$  framework to  $\bar{U}$ – $\bar{V}$  one.

4) *Heading Acquisition*: This step aims to transform  $\bar{\rho}$  to  $\theta$ . We analyze the situations that the robot heading  $\theta$  lies in  $(0, \pi/2]$ ,  $(\pi/2, \pi]$ ,  $(\pi, 3\pi/2]$ , and  $(3\pi/2, 2\pi]$ , respectively. Situation 1 (i.e.,  $(0, \pi/2]$ ) is shown in Fig. 2. It is observed that the camera captures two parallel auxiliary strips that are represented by  $(\bar{r}_1, \bar{\rho}_1)$  and  $(\bar{r}_2, \bar{\rho}_2)$ . Since all auxiliary strips are parallel to the  $X$ -axis,  $\bar{\rho}_1$  equals  $\bar{\rho}_2$  if without considering the measurement error, and therefore, it is sufficient to infer  $\theta$  with the aid of only one auxiliary strip. Select one of  $(\bar{r}_i, \bar{\rho}_i)$  if there are multiple auxiliary strips, and ignore the subscript of  $\bar{\rho}$ . It is easy to derive

$$\theta_{(c1)} = -\bar{\rho} \quad (8)$$

where  $\theta_{(c1)} \in (0, \pi/2]$ . Furthermore, for Situations 2–4, we have

$$\theta_{(c2)} = -\bar{\rho} + \pi \quad (9a)$$

$$\theta_{(c3)} = -\bar{\rho} + \pi \quad (9b)$$

$$\theta_{(c4)} = -\bar{\rho} \quad (9c)$$

where  $\theta_{(c2)} \in (\pi/2, \pi]$ ,  $\theta_{(c3)} \in (\pi, 3\pi/2]$ , and  $\theta_{(c4)} \in (3\pi/2, 2\pi]$ . Combining (8), (9a), (9b), and (9c) together yields

$$\theta \in \{\theta_{(c1)}, \theta_{(c2)}, \theta_{(c3)}, \theta_{(c4)}\} = \{-\bar{\rho}, -\bar{\rho} + \pi\} \quad (10)$$

and consequently, we have

$$\theta \in \begin{cases} \{-\bar{\rho}, -\bar{\rho} + \pi\}, & \text{if } \bar{\rho} \in \left[-\frac{\pi}{2}, 0\right) \\ \{2\pi - \bar{\rho}, -\bar{\rho} + \pi\}, & \text{if } \bar{\rho} \in \left[0, \frac{\pi}{2}\right) \end{cases} \quad (11)$$

which can be used to derive  $\theta$  from  $\bar{\rho}$ .

As seen from the earlier discussion, the visual heading measurement is time-consuming and resource-intensive, so it cannot synchronize with the gyroscopic heading estimation. As  $k = 1, 2, \dots$ , we define sampling point  $t_\ell \in \{1, 2, \dots\}$ , where  $\ell = 1, 2, \dots$ . Define  $\bar{\rho}$  at sampling point  $t_\ell$  by  $\bar{\rho}_{t_\ell}$  and the measurement of  $\bar{\rho}_{t_\ell}$  by  $\bar{\rho}_{c,t_\ell}$ . Since the measurement contains the additive noise, we have

$$\bar{\rho}_{c,t_\ell} = \bar{\rho}_{t_\ell} + n_{c,t_\ell} \quad (12)$$

where  $n_{c,t_\ell}$  denotes the measurement noise. There are many factors causing the measurement noise, such as environmental illumination, misalignment, and camera shake, so the noise statistical characteristics may change with variation of these factors. For example, when the robot enters the area without sufficient light, the performance of image preprocess may degrade, thus causing a heavier noise. Most frequently, the variation is reflected in the noise variance, so we assume  $n_{c,t_\ell} \sim \mathcal{N}(0, R_{t_\ell})$ .

Finally, we obtain the visual heading measurement  $\Theta_{c,t_\ell}$  that is formulated as

$$\Theta_{c,t_\ell} = \begin{cases} \{-\bar{\rho}_{c,t_\ell}, -\bar{\rho}_{c,t_\ell} + \pi\}, & \text{if } \bar{\rho}_{c,t_\ell} \in \left[-\frac{\pi}{2}, 0\right) \\ \{2\pi - \bar{\rho}_{c,t_\ell}, -\bar{\rho}_{c,t_\ell} + \pi\}, & \text{if } \bar{\rho}_{c,t_\ell} \in \left[0, \frac{\pi}{2}\right) \end{cases} \quad (13)$$

which can be rewritten as

$$\Theta_{c,t_\ell} = \begin{cases} \{\theta_{t_\ell} + n_{c,t_\ell}, \theta_{t_\ell} + \pi + n_{c,t_\ell}\}, & \text{if } \theta_{t_\ell} \in [0, \pi) \\ \{\theta_{t_\ell} + n_{c,t_\ell}, \theta_{t_\ell} - \pi + n_{c,t_\ell}\}, & \text{if } \theta_{t_\ell} \in [\pi, 2\pi). \end{cases} \quad (14)$$

It is observed that  $\Theta_{c,t_\ell}$  contains two measurements, a real one  $\theta_{c,t_\ell}^{(\dagger)}$  equalling  $\theta_{t_\ell} + n_{c,t_\ell}$  and a pseudo one  $\theta_{c,t_\ell}^{(\ddagger)}$  equalling  $\theta_{t_\ell} \pm \pi + n_{c,t_\ell}$ . Hence, the robot heading estimation system must have the ability to recognize the pseudomeasurement and isolate it.

### III. INERTIAL-VISUAL FUSION

#### A. Problem Formulation

The inertial-visual fusion problem is based on

$$\theta_{k+1} = \theta_k + T\delta_k \quad (15a)$$

$$\delta_{g,k} = \delta_k + b_{g,k} + n_{g,k} \quad (15b)$$

$$b_{g,k+1} = b_{g,k} + w_{g,k} \quad (15c)$$

$$\Theta_{c,t_\ell} = \begin{cases} \{\theta_{t_\ell} + n_{c,t_\ell}, \theta_{t_\ell} + \pi + n_{c,t_\ell}\}, & \text{if } \theta_{t_\ell} \in [0, \pi) \\ \{\theta_{t_\ell} + n_{c,t_\ell}, \theta_{t_\ell} - \pi + n_{c,t_\ell}\}, & \text{if } \theta_{t_\ell} \in [\pi, 2\pi). \end{cases} \quad (15d)$$

Modifying (15a) to (15d) by state argumentation yields

$$\vartheta_k = F\vartheta_{k-1} + B\delta_{k-1} + Cw_{k-1} \quad (16a)$$

$$\theta_{c,t_\ell} = \begin{cases} \{H\vartheta_{t_\ell} + n_{c,t_\ell}, H\vartheta_{t_\ell} + \pi + n_{c,t_\ell}\}, & \text{if } \theta_{t_\ell} \in [0, \pi) \\ \{H\vartheta_{t_\ell} + n_{c,t_\ell}, H\vartheta_{t_\ell} - \pi + n_{c,t_\ell}\}, & \text{if } \theta_{t_\ell} \in [\pi, 2\pi) \end{cases} \quad (16b)$$

where

$$\vartheta_k = \begin{bmatrix} \theta_k \\ b_{g,k} \end{bmatrix}, \quad w_k = \begin{bmatrix} n_{g,k} \\ w_{g,k} \end{bmatrix} \sim \mathcal{N}(0, Q), \quad Q = \begin{bmatrix} Q_n & 0 \\ 0 & Q_w \end{bmatrix}$$

$$F = \begin{bmatrix} 1 & -T \\ 0 & 1 \end{bmatrix}, \quad B = \begin{bmatrix} T \\ 0 \end{bmatrix}, \quad C = \begin{bmatrix} -T & 0 \\ 0 & 1 \end{bmatrix}, \quad H = \begin{bmatrix} 1 \\ 0 \end{bmatrix}'$$

It is observed that the measurement and state propagation are not in synchronization when  $t_\ell \neq \ell$ . This asynchronization (or multirate) problem is caused by the resource-intensive visual heading measurement. First, the visual heading measurement is accomplished by image acquisition and the subsequent image processing operations, so it costs much more time than the yaw rate measurement that is accomplished by a simple wired data communication with the gyroscope. Second, even the vision and gyroscope could synchronize in hardware, and we may decrease the frequency of the visual heading measurement for the purpose of reducing resource consumption.

The synchronized model of (16a) and (16b) is

$$\vartheta_{t_{\ell+1}} = \mathcal{F}_{t_\ell} \vartheta_{t_\ell} + d_{t_\ell} + \omega_{t_\ell} \quad (17a)$$

$$\theta_{c,t_\ell} = \begin{cases} \{H\vartheta_{t_\ell} + n_{c,t_\ell}, H\vartheta_{t_\ell} + \pi + n_{c,t_\ell}\}, & \text{if } \theta_{t_\ell} \in [0, \pi) \\ \{H\vartheta_{t_\ell} + n_{c,t_\ell}, H\vartheta_{t_\ell} - \pi + n_{c,t_\ell}\}, & \text{if } \theta_{t_\ell} \in [\pi, 2\pi) \end{cases} \quad (17b)$$

where  $\mathcal{F}_{t_\ell} = F^{\zeta_\ell} = \begin{bmatrix} 1 & -\zeta_\ell T \\ 0 & 1 \end{bmatrix}$ ,  $\zeta_\ell = t_{\ell+1} - t_\ell$ ,  $d_{t_\ell} = \sum_{i=t_\ell}^{t_{\ell+1}-1} F^{t_{\ell+1}-i-1} B \delta_i$ , and  $\omega_{t_\ell} = \sum_{i=t_\ell}^{t_{\ell+1}-1} F^{t_{\ell+1}-i-1} C w_i$  is a 2-D Gaussian noise with the covariation  $\mathcal{Q} = \sum_{i=t_\ell}^{t_{\ell+1}-1} F^{t_{\ell+1}-i-1} C Q C' F^{t_{\ell+1}-i-1}$ .

The problem is to develop an inertial-visual heading estimation algorithm based on the gyroscopic readings  $\{\delta_k\}$  and visual measurements  $\{\theta_{c,t_\ell}\}$ . It cannot be easily solved by using a standard Kalman filter because of the following three issues: the existence of pseudomeasurement, varying noise statistical characteristics, and asynchronization between state propagation and measurement.

#### B. Estimation Algorithm

The estimation algorithm contains six steps: initialization, *a priori* estimation, visual measurement trigger, real measurement recognition, *a posteriori* estimation, and noise covariance estimation.

1) *Initialization*: The initial *a posteriori* estimation  $\hat{\vartheta}_0$  should be determined at first, where  $\hat{\vartheta}_0 = [\hat{\theta}_0, \hat{b}_{g,0}]'$ . The initial heading  $\hat{\theta}_0$  is measured artificially, and the initial gyroscopic bias is obtained by averaging the gyroscopic readings in stationary state. The initial *a posteriori* error correlation  $\hat{P}_0$  is initialized by a diagonal matrix with appropriate values.

2) *A Priori Estimation*: Suppose that  $\hat{\vartheta}_{k-1}$  has been obtained, then the *a priori* estimates are achieved by

$$\check{\vartheta}_k = F\hat{\vartheta}_{k-1} + B\delta_{k-1} \quad (18a)$$

$$\check{P}_k = F\hat{P}_{k-1}F' + CQC' \quad (18b)$$

where  $\check{\vartheta}_k$  and  $\vartheta_k$  denotes the *a priori* and *a posteriori* estimations of  $\vartheta_k$ , respectively, and  $\check{P}_k$  and  $\hat{P}_k$  denotes the *a priori* and *a posteriori* estimation error covariances at sampling point  $k$ , respectively.

3) *Visual Measurement Trigger*: The gyroscopic bias (i.e., ARRW) is included in the augmented state as shown in (16a), so it can be estimated and removed in the *a priori* estimation process, which means that the gyroscopic heading estimation is relatively accurate in short term. Hence, to reduce the computational burden, the *a priori* estimation is not necessary

to be corrected at each sampling point until the error variance of heading estimation gets larger than a given bound. The visual measurement is triggered at

$$\tilde{P}_k < \bar{P} \text{ or } H(F\tilde{P}_kF' + CQC')H' + R < \left(\frac{\pi}{2\beta}\right)^2 \quad (19)$$

where  $\beta$  is an integer not less than 3. The function of the first inequation in (19) is to limit the heading estimation error by the upper bound  $\bar{P}$ , whereas the second inequation prevents the real measurement at the next sampling point from being unrecognizable. The discussion of the recognizable condition of real measurement can be found in Appendix A. According to [23],  $\tilde{P}_t$  and  $\hat{P}_t$  converge to time-invariant matrices for a completely observable and completely controllable system. Therefore, the event-based trigger designed earlier will trigger the visual measurement in equal intervals of time after convergence.

4) *Real Measurement Recognition*: If the visual heading measurement is triggered at  $k$ , the real measurement should be recognized. Calculate the  $\theta_{c,k}^{(1)}$ - and  $\theta_{c,k}^{(2)}$ -based innovations  $\phi_k^{(1)}$  and  $\phi_k^{(2)}$  by

$$\phi_k^{(1)} = \theta_{c,k}^{(1)} - H\tilde{\vartheta}_k \quad (20a)$$

$$\phi_k^{(2)} = \theta_{c,k}^{(2)} - H\tilde{\vartheta}_k \quad (20b)$$

where  $\theta_{c,k}^{(1)}$  and  $\theta_{c,k}^{(2)}$  are the elements in  $\Theta_{c,k}$ . The real measurement can be picked out by

$$\theta_{c,k}^{(b)} = \begin{cases} \theta_{c,k}^{(1)}, & \text{if } |\phi_k^{(1)}| < |\phi_k^{(2)}| \\ \theta_{c,k}^{(2)}, & \text{otherwise} \end{cases} \quad (21)$$

where  $\theta_{c,k}^{(b)}$  denotes the recognized real measurement. In Appendix A, we show the recognizable condition of the real measurement, in which  $\theta_{c,k}^{(b)} = \theta_{c,k}^{(\tau)}$  holds in an extreme high probability.

5) *A Posterior Estimation*: If the visual measurement is not triggered, which means that the state propagation and measurement are not synchronized, then the *a posterior* estimates equals the *a priori* estimates, that is,

$$\hat{\vartheta}_k = \tilde{\vartheta}_k \quad (22a)$$

$$\hat{P}_k = \tilde{P}_k \quad (22b)$$

otherwise, the *a posterior* estimate is given by

$$K_k = \tilde{P}_k H' [H\tilde{P}_k H' + \hat{R}_k]^{-1} \quad (23a)$$

$$\hat{\vartheta}_k = \tilde{\vartheta}_k + K_k [\theta_{c,k}^{(b)} - H\tilde{\vartheta}_k] \quad (23b)$$

$$\hat{P}_k = [I_2 - K_k H] \tilde{P}_k \quad (23c)$$

where  $K_k$  denotes the filtering gain at time  $k$ , and  $I_2$  denotes the 2-D unit matrix.

6) *Noise Covariance Estimation*: Define another time stamp  $t_\ell^\tau$  where  $\tau$  is set as 0 initially. When  $\varsigma_\ell = \varsigma_{\ell-1}$  and  $\varsigma_{\ell-3} = \varsigma_{\ell-4}$ , we increase  $\tau$  by 1, calculate  $\nabla\Theta_{c,t_\ell}^{(b)} = \theta_{c,t_\ell}^{(b)} - 2\theta_{c,t_{\ell-1}}^{(b)} + \theta_{c,t_{\ell-2}}^{(b)} - T\bar{\delta}_{g,t_{\ell-1}} + T\bar{\delta}_{g,t_{\ell-2}}$  where  $\bar{\delta}_{g,t_\ell} = \sum_{i=t_\ell}^{t_{\ell+1}-1} \delta_{g,i}$ , and assign the value of  $\nabla\Theta_{c,t_\ell}^{(b)} \cdot \nabla\Theta_{c,t_{\ell-2}}^{(b)}$  to  $\mathcal{I}_{t_\ell}^\tau$ . Finally, the measurement noise variance is estimated by

$$\hat{R}_{t_\ell}^\tau = \hat{R}_{t_\ell}^{\tau-1} + \frac{1}{n}(\mathcal{I}_{t_\ell}^\tau - \mathcal{I}_{t_\ell}^{\tau-1-n}) \quad (24)$$

---

### Algorithm 1 Pseudomeasurement-Resistant Adaptive Asynchronous Kalman Filter

---

- 1: Initialize  $\hat{\vartheta}_0, \hat{P}_0, \hat{R}_0$
  - 2: **for**  $k = 1 : \infty$  **do**
  - 3:  $\tilde{\vartheta}_k = F\tilde{\vartheta}_{k-1} + B\delta_{k-1}, \tilde{P}_k = F\tilde{P}_{k-1}F' + CQC'$
  - 4: **if**  $\tilde{P}_k < \bar{P}$  or  $H(F\tilde{P}_kF' + CQC')H' + R < (\frac{\pi}{2\beta})^2$  **then**
  - 5:  $\phi_k^{(1)} = \theta_{c,k}^{(1)} - H\tilde{\vartheta}_k, \phi_k^{(2)} = \theta_{c,k}^{(2)} - H\tilde{\vartheta}_k$
  - 6:  $\theta_{c,k}^{(b)} = \begin{cases} \theta_{c,k}^{(1)}, & \text{if } |\phi_k^{(1)}| < |\phi_k^{(2)}|, \\ \theta_{c,k}^{(2)}, & \text{otherwise,} \end{cases}$
  - 7:  $K_k = \tilde{P}_k H' [H\tilde{P}_k H' + \hat{R}_k]^{-1}$
  - 8:  $\hat{\vartheta}_k = \tilde{\vartheta}_k + K_k [\theta_{c,k}^{(b)} - H\tilde{\vartheta}_k], \hat{P}_k = [I_2 - K_k H] \tilde{P}_k$
  - 9:  $\hat{R}_{t_\ell}^\tau = \hat{R}_{t_\ell}^{\tau-1} + \frac{1}{n}(\mathcal{I}_{t_\ell}^\tau - \mathcal{I}_{t_\ell}^{\tau-1-n})$
  - 10: **else**
  - 11:  $\hat{\vartheta}_k = \tilde{\vartheta}_k, \hat{P}_k = \tilde{P}_k$
  - 12: **end if**
  - 13: **end for**
- 

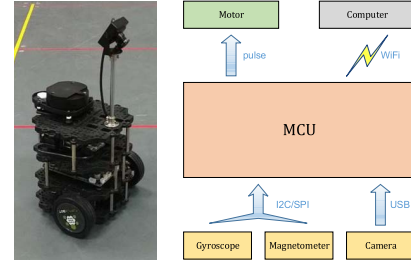


Fig. 3. Description of the experimental robot.

where  $\tau > n$ . At the starting phase, there may not be a sufficient number of  $\mathcal{I}_{t_\ell}^\tau$ , i.e.,  $\tau \leq n$ , and thus, the measurement noise variance can be  $\hat{R}_{t_\ell}^\tau = (1/\tau) \sum_{i=t_\ell}^{t_\ell} \mathcal{I}_i$ . The derivation of (24) can be found in Appendix B. Furthermore, it is noted that  $\hat{R}_{t_\ell}^\tau$  should not be introduced to the filter at each  $t_\ell^\tau$  for the reason that a varying  $\hat{R}_{t_\ell}^\tau$  leads to a varying  $\varsigma_\ell$ , thus causing a smaller number of  $\mathcal{I}_{t_\ell}^\tau$ . The pseudomeasurement-resistant adaptive asynchronous Kalman filter is summarized in Algorithm 1.

## IV. EXPERIMENTAL VERIFICATION

### A. Experiment Setup

As shown in Fig. 3, the experimental robot (Turtlebot3 Burger) is mounted with a camera looking downward to the floor that is covered with red parallel auxiliary strips. All these auxiliary strips are equally spaced by 0.5 m and parallel to the X-axis. Other sensors, such as gyroscopes, are embedded on the circuit board. The key information of the sensors is shown in Table I.

The implementation of the proposed system is not demanding to have expensive dedicated gyroscope or camera. As an example, we use a customer-grade MEMS gyroscope, the type of which is MPU6050 (manufactured by InvenSense, less than U.S. \$1 per chip), to perceive the yaw rate. The other gyroscope, ADXR453, has higher accuracy than MPU6050,

TABLE I  
INFORMATION OF THE SENSORS

Sensor	Information
Gyroscope	MPU6050, range: $\pm 250$ deg/s; initial ZRO* tolerance: $\pm 5$ deg/s; total RMS** noise: 0.1 deg/s.
Gyroscope	ADXRS453, range: $\pm 400$ deg/s; accuracy: $\pm 0.4$ deg/s.
Magnetometer	AK8963, range: $\pm 4800$ uT.
Camera	RMONCAM, normal lens; resolution: $480 \times 640$ ; rate: 30 fps.

\* Zero-Rate Output; \*\* Root Mean Square.

so it is used to provide the truth values of heading angles but not to participate in the proposed HDS. In addition, we use a general-purpose full-color camera, the resolution of which is  $640 \times 480$  (less than U.S. \$10 per piece), to capture the floor image. All sensors work at 10 Hz. Algorithms are coded by python and executed on an integrated development environment called Spyder.

### B. Evaluation of the Proposed HDS

1) *Pseudomeasurement Isolation*: The estimation results of the proposed HDS within the first 500 sampling points are shown in Fig. 4. The initial setup follows:  $\hat{\vartheta}_0 = [90.5, 1.7]'$ ,  $Q = \text{diag}(0.38^2, 0.05^2)$ , and  $R = 1.4^2$ . It is observed that two measurements (the real one and pseudo one) exist, but the pseudomeasurement can be isolated correctly all the time, and consequently, the heading estimation tracks the truth with high accuracy. As shown in Fig. 4(a), the visual heading measurement is triggered by 25 times during the 500 sampling points, and the heading estimation achieves the smallest root-mean-square error (RMSE) of  $0.98^\circ$ . As shown in Fig. 4(b) and (c), the period without visual correction gets longer with  $\bar{P}$  increasing, thus causing larger RMSEs. It can also be observed, however, that the pseudomeasurements are always outside the range of innovation boundary  $[-3(H\tilde{P}_tH' + R_t)^{1/2}, +3(H\tilde{P}_tH' + R_t)^{1/2}]$ , while the real ones inside, provided that the visual heading measurement is triggered in time. Finally, observing the visual measurements (blue crossings), their intervals get larger and remain fixed over time for the filtering convergence. Hence, we can conclude that the accuracy increases with the frequencies of data sampling and visual correction increasing and the stability could be kept under timely visual correction, i.e., the frequency of visual heading measurement should be higher than a critical one, which could be calculated according to the recognizable condition in Appendix A.

2) *Noise Variance Estimation*: At the sampling point of about 11 000, we dim the light and loose the screws that fix the downward-looking camera, thus causing an increase of the noise variance of the visual heading measurement. The initial  $\bar{P} = 2^2$ ,  $R = 1.4^2$ , and the sliding window width of  $\hat{R}_{t_i}$  equals 500. If the noise variance  $R$  is not adjusted, then the heading estimation RMSE is  $2.71^\circ$ . After introducing the noise variance estimator, the RMSE is reduced to  $1.57^\circ$ . The real  $R$  changes from 2 to 10 after the environmental variation, which coincide approximately with the performance of the  $R$  estimator, as shown in Fig. 5. It is also interesting

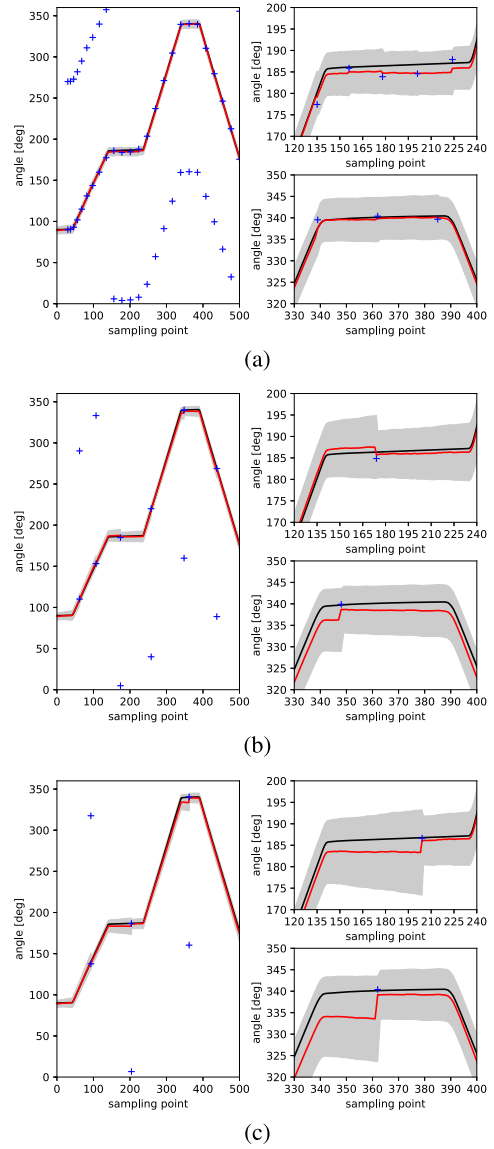


Fig. 4. Estimation results of the proposed HDS. The black curves ( $\sim$ ) stand for the truth values, the red curves ( $\sim$ ) stand for the estimates, the blue crossings ( $+$ ) stand for the measurements, and the gray areas stand for the innovation boundaries. (a) Heading estimation results under  $\bar{P} = 1^2$ . RMSE =  $0.98^\circ$ . (b) Heading estimation results under  $\bar{P} = 2^2$ . RMSE =  $1.56^\circ$ . (c) Heading estimation results under  $\bar{P} = 3^2$ . RMSE =  $2.57^\circ$ .

to observe that the visual heading measurement is triggered more and more frequently until  $\hat{R}_{t_i}$  converges. According to the recognizable condition of real measurement, if  $R$  increases and the HDS works at a low correction rate, and then, the heading estimation may be invalid due to the confusion in distinguishing the real and pseudomeasurements. In our design, however, an increasing  $R$  leads to a more frequent visual correction, thus accelerating the convergence of  $\hat{R}_{t_i}$ . Because of the introduction of noise variance estimation, the proposed HDS could adapt to illumination variation and camera vibration.

### C. Comparative Study

The experimental environment with interferences is established by placing some ferromagnetic materials such as iron

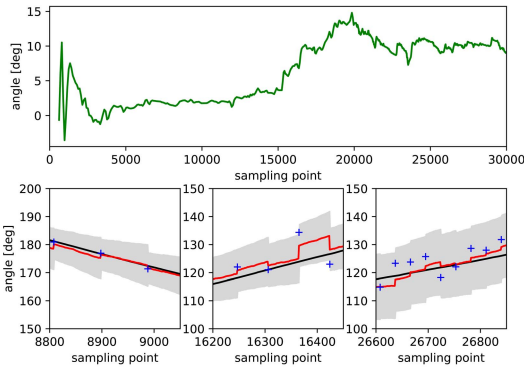


Fig. 5. Experiment results when introducing noise variance estimator. The green curves stand for the estimated  $R$ . RMSE =  $1.57^\circ$ .

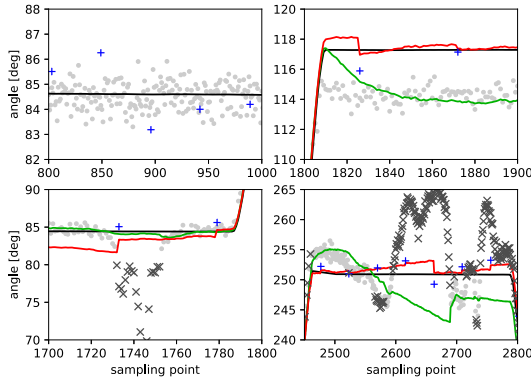


Fig. 6. Results of comparative study with a magnetic HDS. The green curves stand for the outputs of the magnetic HDS, whereas the red curves stand for the outputs of the proposed nonmagnetic HDS. The dots in light gray stand for the outputs of the magnetic compass, while the crossings in deep gray stand for the recognized anomalies.

weights. A magnetic HDS is composed of a gyroscope and a magnetic compass (usually a magnetometer) and outputs the heading estimation by fusing the readings of the two complementary sensors. In [9], an advanced gyroscope-magnetometer-integrated algorithm is proposed. The algorithm could recognize and isolate the ferro- or electro-interference-induced anomalies in magnetic compass. The comparative results are shown in Fig. 6. In the case without interference, the magnetic compass performs in a stable and accurate manner as the top-left subfigure exhibited. As the bottom-left subfigure exhibited, if the interference incurs a sudden variation to the magnetic compass, then these anomalies could be recognized accurately and isolated, and thus, the heading estimation is not affected. However, the bias is small or turns to larger in a gradual way, and the anomalies cannot be recognized. Because the Kalman filter tracks the measurements, the unrecognized anomalies give rise to the failure of magnetic heading estimation, exactly as the up- and down-right subfigures exhibited. In conclusion, the ferromagnetic and electromagnetic interferences cause the potential performance instability to a magnetic HDS that involves a magnetometer, but do not affect the proposed nonmagnetic one.

## V. CONCLUSION AND DISCUSSION

In this brief, a structurally simple yet efficient nonmagnetic HDS has been developed, which can be used in the planar

indoor environment with abundant ferromagnetic and electromagnetic interferences, by the combination of gyroscope and vision. As the experiments shown, such a visual-inertial HDS, coupled with the proposed pseudomeasurement-resistant adaptive asynchronous Kalman filter, could isolate the pseudomeasurement accurately and adapt to the environmental variation by estimating the measurement noise variance. Furthermore, as a nonmagnetic way to determine the robot heading, the developed system provides an effective alternative solution in the environments with abundant magnetic interferences.

Here are some discussions about the sensors. The main parameter of gyroscope is the root-mean-square (rms) noise. If rms noise is smaller, then the gyroscopic heading estimation could provide an accurate estimation in longer time, and therefore, the visual measurement is triggered in lower frequency, which means a lower computational burden. The main parameters of camera are lens distortion and resolution. In fact, the resolution does not affect the visual measurement significantly, but the lens distortion does. The accuracy of visual measurement decreases with lens distortion degree increasing. In conclusion, a gyroscope with lower rms noise and a camera with lower lens distortion are preferred in practice.

## APPENDIX A

Define the innovations based on  $\theta_{c,t}^{(\dagger)}$  and  $\theta_{c,t}^{(\ddagger)}$  by

$$\phi_{t}^{(\dagger)} = \theta_{c,t}^{(\dagger)} - H\tilde{v}_{t} \quad (25a)$$

$$\phi_{t}^{(\ddagger)} = \theta_{c,t}^{(\ddagger)} - H\tilde{v}_{t} = \pm\pi + \phi_{t}^{(\dagger)} \quad (25b)$$

which are Gaussian noises.  $\phi_{t}^{(\dagger)}$  is a Gaussian white noise, i.e.,  $\phi_{t}^{(\dagger)} \sim \mathcal{N}(0, H\tilde{P}_{t}H' + R_{t})$ , and  $\phi_{t}^{(\ddagger)}$  is a colored one, i.e.,  $\phi_{t}^{(\ddagger)} \sim \mathcal{N}(\pm\pi, H\tilde{P}_{t}H' + R_{t})$ . Obviously,  $\phi_{t}^{(\dagger)}$  and  $\phi_{t}^{(\ddagger)}$  are not independently and identically distributed but differ by an offset  $\pm\pi$ . If it is desired that  $|\phi_{t}^{(\dagger)}| < |\phi_{t}^{(\ddagger)}| = |\pm\pi + \phi_{t}^{(\dagger)}|$  holds, then  $|\phi_{t}^{(\dagger)}| \leq \pi/2$  is expected. Since  $\phi_{t}^{(\dagger)} \sim \mathcal{N}(0, H\tilde{P}_{t}H' + R_{t})$ ,  $|\phi_{t}^{(\dagger)}| \leq \pi/2$  cannot hold always but can hold in an extremely high probability. For example, if  $\pi/2 \geq 3(H\tilde{P}_{t}H' + R_{t})^{1/2}$ , then  $\mathcal{P}(|\phi_{t}^{(\dagger)}| \leq \pi/2) \geq 99.73\%$ , which means that the real measurement derived innovation is greater than the pseudo one in a probability of 99.73%. The probability can be increased by increasing the multiple of  $(H\tilde{P}_{t}H' + R_{t})^{1/2}$ . Therefore, the recognizable condition is  $\pi/2 \geq \beta(H\tilde{P}_{t}H' + R_{t})^{1/2}$ , where  $\beta > 0$  is a parameter which is generally set as an integer greater than 3.

## APPENDIX B

The difference series of  $\theta_{c,t}^{(b)}$  contain  $w_{g,k}$ ,  $n_{g,k}$ , and  $n_{c,t}$ , which enables the estimation of noise variances. Consider the following equations:

$$\theta_{t+1} = \theta_t + T \sum_{i=t}^{t+1-1} (\delta_{g,i} - b_{g,i} - n_{g,i}) \quad (26a)$$

$$\theta_{c,t+1}^{(b)} = \theta_{t+1} + n_{c,t+1} \quad (26b)$$

$$\theta_{c,t}^{(b)} = \theta_t + n_{c,t} \quad (26c)$$

and define  $\bar{\delta}_{g,t_\ell} = \sum_{i=t_\ell}^{t_{\ell+1}-1} \delta_{g,i}$ ,  $\bar{b}_{g,t_\ell} = \sum_{i=t_\ell}^{t_{\ell+1}-1} b_{g,i}$ , and  $\bar{n}_{g,t_\ell} = \sum_{i=t_\ell}^{t_{\ell+1}-1} n_{g,i}$ . Subtracting (26b) from (26c) yields

$$\begin{aligned} \theta_{c,t_{\ell+1}}^{(b)} - \theta_{c,t_\ell}^{(b)} &= \theta_{t_{\ell+1}} + n_{c,t_{\ell+1}} - \theta_{t_\ell} - n_{c,t_\ell} \\ &= T(\bar{\delta}_{g,t_\ell} - \bar{b}_{g,t_\ell} - \bar{n}_{g,t_\ell}) + n_{c,t_{\ell+1}} - n_{c,t_\ell} \end{aligned} \quad (27)$$

and then yields

$$\begin{aligned} \Theta_{c,t_{\ell+1}}^{(b)} &= \theta_{c,t_{\ell+1}}^{(b)} - \theta_{c,t_\ell}^{(b)} - T\bar{\delta}_{g,t_\ell} \\ &= n_{c,t_{\ell+1}} - n_{c,t_\ell} - T\bar{b}_{g,t_\ell} - T\bar{n}_{g,t_\ell} \end{aligned} \quad (28)$$

which includes the gyroscopic and visual error terms. For removing  $\bar{b}_{g,t_\ell}$ , the backward difference operator  $\nabla$  is introduced. If  $\varsigma_\ell = \varsigma_{\ell-1}$ , then we have

$$\begin{aligned} \nabla \Theta_{c,t_{\ell+1}}^{(b)} &= \Theta_{c,t_{\ell+1}}^{(b)} - \Theta_{c,t_\ell}^{(b)} \\ &= \theta_{c,t_{\ell+1}}^{(b)} - 2\theta_{c,t_\ell}^{(b)} + \theta_{c,t_{\ell-1}}^{(b)} - T\bar{\delta}_{g,t_\ell} + T\bar{\delta}_{g,t_{\ell-1}} \\ &= n_{c,t_{\ell+1}} - 2n_{c,t_\ell} + n_{c,t_{\ell-1}} - T(\bar{b}_{g,t_\ell} - \bar{b}_{g,t_{\ell-1}}) \\ &\quad - T(\bar{n}_{g,t_\ell} - \bar{n}_{g,t_{\ell-1}}) \\ &= n_{c,t_{\ell+1}} - 2n_{c,t_\ell} + n_{c,t_{\ell-1}} - T\bar{w}_{g,t_{\ell-1}} \\ &\quad - T(\bar{n}_{g,t_\ell} - \bar{n}_{g,t_{\ell-1}}) \end{aligned} \quad (29)$$

where  $\bar{w}_{g,t_{\ell-1}} = \sum_{j=t_{\ell-1}}^{t_\ell-1} \sum_{i=j}^{j+\varsigma_\ell-1} w_{g,i}$ .

It is observed that (29) is the sum of three moving average stochastic processes  $\bar{w}_{g,t_{\ell-1}}$ ,  $\bar{n}_{g,t_\ell} - \bar{n}_{g,t_{\ell-1}}$ , and  $n_{c,t_{\ell+1}} - 2n_{c,t_\ell} + n_{c,t_{\ell-1}}$ . Calculating the correlation functions of the left- and right-hand sides of (29) yields

$$A = \mathbb{E}[\nabla \Theta_{c,t_\ell}^{(b)} \cdot \nabla \Theta_{c,t_{\ell-2}}^{(b)}] = R \quad (30)$$

where  $\mathbb{E}$  denotes the mathematical expectation. Because  $\nabla \Theta_{c,t_{\ell+1}}^{(b)}$  only holds at  $\varsigma_\ell = \varsigma_{\ell-1}$ ,  $\nabla \Theta_{c,t_\ell}^{(b)} \cdot \nabla \Theta_{c,t_{\ell-2}}^{(b)}$  only exists at  $\varsigma_\ell = \varsigma_{\ell-1}$  and  $\varsigma_{\ell-3} = \varsigma_{\ell-4}$ . Define another time stamp  $t_\ell^\tau \in \{t_\ell, \ell = 1, 2, \dots\}$ , where  $\tau = 1, 2, \dots$ . When  $\varsigma_\ell = \varsigma_{\ell-1}$  and  $\varsigma_{\ell-3} = \varsigma_{\ell-4}$ , we increase  $\tau$  by 1, assign the value of  $t_\ell$  to  $t_\ell^\tau$ , and let  $\mathcal{I}_{t_\ell^\tau} = \nabla \Theta_{c,t_\ell}^{(b)} \cdot \nabla \Theta_{c,t_{\ell-2}}^{(b)}$ . Finally, the measurement noise variance is estimated by

$$\begin{aligned} \widehat{R}_{t_\ell^\tau} &= \frac{1}{n} \sum_{i=t_\ell^\tau-n}^{t_\ell^\tau} \mathcal{I}_i = \frac{1}{n} \left( \sum_{i=t_\ell^\tau-1-n}^{t_\ell^\tau-1} \mathcal{I}_i + \mathcal{I}_{t_\ell^\tau} - \mathcal{I}_{t_\ell^\tau-1-n} \right) \\ &= \widehat{R}_{t_\ell^\tau-1} + \frac{1}{n} (\mathcal{I}_{t_\ell^\tau} - \mathcal{I}_{t_\ell^\tau-1-n}) \end{aligned} \quad (31)$$

when  $\tau > n$ ; otherwise,  $\widehat{R}_{t_\ell^\tau} = (1/\tau) \sum_{i=t_\ell^\tau}^{t_\ell^\tau} \mathcal{I}_i$ .

## REFERENCES

[1] R. Siegwart, I. R. Nourbakhsh, and D. Scaramuzza, *Introduction to Autonomous Mobile Robots*, 2nd ed. Cambridge, MA, USA: MIT Press, 2011.

[2] M. Chen, P. Shi, and C.-C. Lim, "Robust constrained control for MIMO nonlinear systems based on disturbance observer," *IEEE Trans. Autom. Control*, vol. 60, no. 12, pp. 3281–3286, Dec. 2015.

[3] M. Chen, "Disturbance attenuation tracking control for wheeled mobile robots with skidding and slipping," *IEEE Trans. Ind. Electron.*, vol. 64, no. 4, pp. 3359–3368, Apr. 2017.

[4] W. Lv, Y. Kang, and Y.-B. Zhao, "FVC: A novel nonmagnetic compass," *IEEE Trans. Ind. Electron.*, vol. 66, no. 10, pp. 7810–7820, Oct. 2019.

[5] W. Lv, Y. Kang, and Y. Zhao, "Self-tuning asynchronous filter for linear Gaussian system and applications," *IEEE/CAA J. Autom. Sinica*, vol. 5, no. 6, pp. 1054–1061, Nov. 2018.

[6] W. Lowrie, *Fundamentals of Geophysics*. Cambridge, U.K.: Cambridge Univ. Press, 2007.

[7] J. Fang, H. Sun, J. Cao, X. Zhang, and Y. Tao, "A novel calibration method of magnetic compass based on ellipsoid fitting," *IEEE Trans. Instrum. Meas.*, vol. 60, no. 6, pp. 2053–2061, Jun. 2011.

[8] H.-Y. Chung, C.-C. Hou, and Y.-S. Chen, "Indoor intelligent mobile robot localization using fuzzy compensation and Kalman filter to fuse the data of gyroscope and magnetometer," *IEEE Trans. Ind. Electron.*, vol. 62, no. 10, pp. 6436–6447, Oct. 2015.

[9] W. Lv, Y. Kang, and J. Qin, "Indoor localization for skid-steering mobile robot by fusing encoder, gyroscope, and magnetometer," *IEEE Trans. Syst., Man, Cybern. Syst.*, vol. 49, no. 6, pp. 1241–1253, Jun. 2019.

[10] C.-H. Tu, K. Y. Tu, F.-R. Chang, and L.-S. Wang, "GPS compass: Novel navigation equipment," *IEEE Trans. Aerosp. Electron. Syst.*, vol. 33, no. 3, pp. 1063–1068, Jul. 1997.

[11] J.-C. Juang and C.-F. Lin, "A sensor fusion scheme for the estimation of vehicular speed and heading angle," *IEEE Trans. Veh. Technol.*, vol. 64, no. 7, pp. 2773–2782, Jul. 2015.

[12] T. A. Riggs, T. Inanc, and W. Zhang, "An autonomous mobile robotics testbed: Construction, validation, and experiments," *IEEE Trans. Control Syst. Technol.*, vol. 18, no. 3, pp. 757–766, May 2010.

[13] J. P. How, B. Behihke, A. Frank, D. Dale, and J. Vian, "Real-time indoor autonomous vehicle test environment," *IEEE Control Syst.*, vol. 28, no. 2, pp. 51–64, Apr. 2008.

[14] S. Hoermann and P. V. K. Borges, "Vehicle localization and classification using off-board vision and 3-D models," *IEEE Trans. Robot.*, vol. 30, no. 2, pp. 432–447, Apr. 2014.

[15] P. Nazemzadeh, D. Fontanelli, D. Macii, and L. Palopoli, "Indoor localization of mobile robots through QR code detection and dead reckoning data fusion," *IEEE/ASME Trans. Mechatronics*, vol. 22, no. 6, pp. 2588–2599, Dec. 2017.

[16] E. Guizzo, "Three engineers, hundreds of robots, one warehouse," *IEEE Spectr.*, vol. 45, no. 7, pp. 26–34, Jul. 2008.

[17] Y. Li, L. Ding, and G. Liu, "Error-tolerant switched robust extended Kalman filter with application to parameter estimation of wheel-soil interaction," *IEEE Trans. Control Syst. Technol.*, vol. 22, no. 4, pp. 1448–1460, Jul. 2014.

[18] Y. Li, Y. Tan, R. Dong, and H. Li, "State estimation of macromotion positioning tables based on switching Kalman filter," *IEEE Trans. Control Syst. Technol.*, vol. 25, no. 3, pp. 1076–1083, May 2017.

[19] M. Partovibakhsh and G. Liu, "An adaptive unscented Kalman filtering approach for online estimation of model parameters and state-of-charge of lithium-ion batteries for autonomous mobile robots," *IEEE Trans. Control Syst. Technol.*, vol. 23, no. 1, pp. 357–363, Jan. 2015.

[20] J. K. Bekkeng, "Calibration of a novel MEMS inertial reference unit," *IEEE Trans. Instrum. Meas.*, vol. 58, no. 6, pp. 1967–1974, Jun. 2009.

[21] H. Chang, L. Xue, C. Jiang, M. Kraft, and W. Yuan, "Combining numerous uncorrelated MEMS gyroscopes for accuracy improvement based on an optimal Kalman filter," *IEEE Trans. Instrum. Meas.*, vol. 61, no. 11, pp. 3084–3093, Nov. 2012.

[22] R. Szeliski, *Computer Vision: Algorithms and Applications*. London, U.K.: Springer-Verlag, 2010.

[23] C. K. Chui and G. Chen, *Kalman Filtering: With Real-Time Applications*. Springer, 2017.